Macromolecules **2002,** *35,* 5153−5160

Phase Separation in Ternary Polymer Solutions Induced by Solvent Loss

Ian Hopkinson* and Matthew Myatt

Cavendish Laboratory, University of Cambridge, Madingley Road,
Cambridge CB3 0HE, United Kingdom

Received December 27, 2001

ABSTRACT: Laser scanning confocal microscopy and image analysis have been used to study the phase separation behavior of ternary solutions of dextran, poly(ethylene glycol), and water during drying. The morphology development is strongly affected by the inhomogeneous nature of the solvent quench and by gravitational sedimentation. A range of transient structures is seen in which the morphology varies with depth into the sample. The origin and development of these structures are explained using simple models. For mixtures where the overall volume fraction of the dextran-rich phase, ϕ_s, is 0.1 or 0.34 a droplet morphology is observed whose development is analyzed in detail. The mean radius of the largest droplets is found to increase linearly with time. For mixtures with $\phi_s = 0.5$, a bicontinuous morphology is seen in which the characteristic length scale decreases with depth into the sample as a result of the inhomogeneous distribution of water in the drying film.

Introduction

Phase separation in polymer blends and solutions is of great technological and theoretical interest. Such systems have been widely used for studies of phase separation as the characteristic length and time scales are large compared to other “model” systems of phase separation, such as binary metals and simple liquids. The mechanisms of phase separation are therefore more experimentally accessible. However, because of the nature of polymers and their solutions, hydrodynamic effects are often significant, thus increasing the complexity of these systems.

In the vast majority of phase separation studies of polymer solutions, the experiment involves a “homogeneous” (i.e., spatially invariant) step quench, often of temperature. In industrial polymer processing, however, quenches are often nonuniform; for example, thermal gradients are a feature of most melt processing methods. Solvent quenching, which occurs in such important processes as spin-coating, film-casting, spray-drying, and freeze-drying, has received little scientific attention. Because of the very nature of solvent loss, which occurs at the sample−air interface, solvent quenches will usually be inhomogeneous, leading to variations of solvent concentration within the sample. A further complication of drying processes is that solvent loss is *continuous*, and hence the equilibrium phase compositions are constantly changing. It is clearly of great importance to understand the effect of such “nonideal” quenches on the morphology and the resulting properties of phase-separated blends. This investigation is intended to probe these effects.

In this work, we study the evolution of phase-separated morphologies in films of an aqueous ternary polymer mixture undergoing drying. Films with a range of initial compositions were dried, under a controlled flow of dry nitrogen, at different rates. While drying, the films were noninvasively imaged in three dimensions using laser scanning confocal microscopy.

Previous studies of dried films of ternary polymer solutions by Kumacheva,[1] Mitov,[2] Serrano,[3] and Müller-Buschbaum[4] have focused on the final morphology of a dried layer. Kumacheva and Mitov, studying films formed by the evaporation of polystyrene/poly(methyl methacrylate)/toluene, found regular arrays of droplets of one phase at the air−film interface above a layer depleted in that phase; they attributed this behavior to Benard−Marangoni convection. Müller-Buschbaum, on the other hand, concentrated on the surface topology of films prepared by the drying of polystyrene/poly(bromostyrene)/solvent solutions using a wide range of solvents to study their effect on the final morphology. In this work we look at the dynamics of the drying process to establish mechanisms of phase coarsening in this type of system. This gives us access to further transient structures which are not probed in studies of final film morphology.

In general, the presence of gravitational effects in the late stages of phase separation has been a confounding factor in the study of phase separation. Studies have been performed on the structural evolution of phase-separated systems following vigorous stirring,[5,6] which essentially amounts to a sedimentation process. These studies find a moving front between the two final phases, with a distribution of droplet sizes close to the front. The size of droplets is greater close to the moving front, but their growth is limited at long times by hydrodynamic effects. The characteristic demixing time is found to scale with the reduced temperature.

Phase separation occurring in a gravitational field has been examined in a number of studies involving both simulation[7,8] and experiment.[9] Puri[7] sought anisotropy in the early stages of phase separation and explicitly excluded the effects of gravitational sedimentation. Lacasta[8] focused on the evolution of a critical mixture in the context of model B, i.e., with no hydrodynamics. Lattice Boltzmann simulations of fluid flow and phase

---

* To whom correspondence should be addressed. Current address: Department of Physics, UMIST, P.O. Box 88, Manchester M60 1QD, U.K. E-mail: I.Hopkinson@umist.ac.uk, fax +44 (0)-161 200 3941.

10.1021/ma012244p CCC: $22.00

separation[10,11] clearly have the potential to model the system we have; however, to date, calculations appear not to have been done. Therefore, these simulation studies, although interesting, are not directly relevant to the behavior we observe. There have also been studies of phase separation in the presence of temperature gradients, for example Assenheimer[12] and Platten.[13] Assenheimer found a wide range of morphologies depending on the applied temperature gradient in the direction of gravity, while Platten applied a temperature gradient in the horizontal direction. In both cases the thermally driven convection was strong and dominated the behavior; in this work, we anticipate rather weaker effects driven by a water concentration gradient.

Laser scanning confocal microscopy[14−16] (LSCM) is an optical microscopy whose key feature is the exclusion of out of focus light from the final image by the use of a "confocal" pinhole in the detection pathway. Consequently, the image obtained is a very thin "optical section" through the specimen at the focal plane. By taking a series of 2D optical sections at different depths in the specimen, a 3D image can be built up. Such 3D imaging is invaluable to the current investigation, allowing the morphology development throughout the whole depth of the film to be studied. The noninvasive nature of the imaging process is also important, permitting the in situ observation of films during drying.

LSCM has been used extensively in the biological sciences, where fluorescent labeling of particular cell components is a very powerful tool, and there is always a need to achieve higher resolution to image ever smaller biological structures. In the physical sciences, LSCM has been used rather less, although there is a growing community of users. Particularly notable are the studies of colloidal materials by van Blaaderen et al.[17,18] and phase-separated morphology in polymer systems by Ribbe et al.,[19,20] Jinnai et al.,[21−23] and Takeno.[24] In these experiments fluorescence labeling has been key because refractive index contrast is difficult to engineer. Furthermore, techniques such as differential interference contrast and phase contrast that are often used in materials science studies are difficult to achieve in LSCM due, in part, to the thickness of the sample and the complexity of the necessary optics.

While LSCM is undoubtedly a very valuable tool for the study of phase separation in polymeric systems, its limited length- and time-scale resolution mean that it cannot be used to study the early stage of phase separation (usually defined as the period $0.1 < q\xi < 1.0$, where q is the scattering vector for the characteristic length scale and ξ is the correlation length). In this study, the smallest structures that can be resolved have a length scale of around 1.8 μm, giving a maximum value of q of 3.5 μm^{-1}. The correlation length is of the order of 10 nm, as we are typically far from the critical point, and so the maximum value of $q\xi$ is approximately 0.035. Consequently, the structure developments described in this work are related to late-stage coarsening processes.

Experimental Section

Dextran (M_w = 148 000, Sigma D-4876) and poly(ethylene glycol) (PEG) (M_w = 8000, Sigma P-4463) were purchased and used as received. In all experiments, the dextran was fluorescently labeled by the addition of 1.0 wt % fluorescein isothiocyanate (FITC)−dextran conjugate (M_w = 150 000, FITC: glucose = 1:160, Fluka 46946).

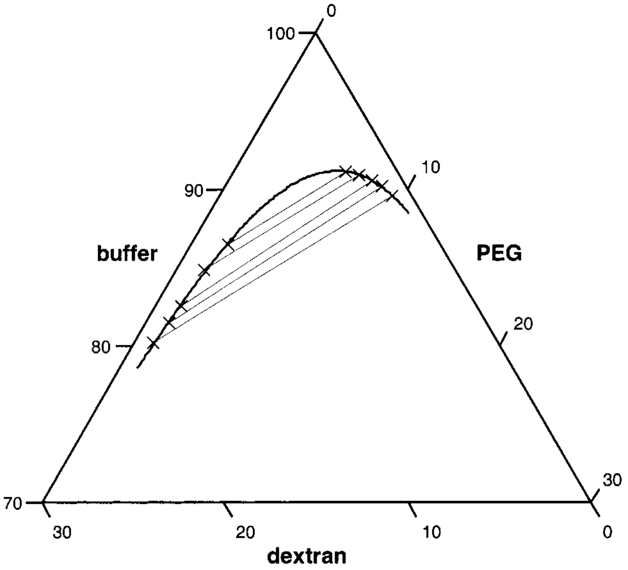

Figure 1. Phase diagram for the dextran/PEG/buffer system axes in terms of weight percentage polymer.

Figure 1 shows the phase diagram for our system, obtained using UV/vis spectrometry; we will describe these results in more detail elsewhere. These results for fluorescently labeled polymers are consistent with phase diagrams for dextran/PEG/water solutions published in Zaslavsky.[25]

Solutions of dextran, PEG, and water were prepared with three different dextran:PEG ratios. The ratios were set so that, when macroscopically phase separated, the equilibrium volume fraction of the dextran-rich phase, ϕ_s, equaled 0.1, 0.34, and 0.5. The water content was then adjusted so that each solution was in the single-phase region, just above the coexistence curve. The solutions were stirred for a minimum of 24 h to ensure complete mixing.

A fixed volume of solution was injected into a 30 mm diameter polystyrene Petri dish to give a film with an initial thickness of 245 ± 15 μm. The sample was placed onto the stage of a Zeiss LSM 510 upright confocal microscope ready for observation with a ×20 dry objective lens (NA 0.5). A higher resolution oil-immersion lens could not be used in this study as the surface of the film had to open to the atmosphere to allow evaporation. The use of such a lens, which would allow observations of morphology on a much smaller scale, might be possible if an inverted microscope is used. The sample and objective lens were surrounded with a polycarbonate enclosure through which dry nitrogen was passed at a known flow rate. Drying rate was varied by altering the flow rate of the nitrogen. A pipe heater was used to keep the temperature of the nitrogen flow at 22 ± 1 °C. To minimize mass transport in the sample within the horizontal (x, y) directions, the microscope stage was carefully leveled so the sample was horizontal. The meniscus between the film and the sides of the Petri dish extended only a few millimeters away from the dish, leaving a large area in the middle of the film where the surface was flat.

The film was imaged several times as it dried. Contrast was provided by the FITC−dextran component which was excited using the 488 nm line of the microscope's argon ion laser. Reflected light was excluded by the use of a long-pass 505 nm filter. 3D image stacks covering the entire depth of the film were captured at intervals of 1 min or more. Each image stack consisted of 30 horizontal image slices with 256 × 256 pixels and covering an area of 230 μm × 230 μm. The vertical spacing of the image slices was gradually reduced during the experiment, as the sample became thinner due to water loss, typically ranging between 11 and 6 μm. The thickness of the focal plane, which depends on the numerical aperture of the objective lens and the pinhole diameter, was approximately 5.3 μm. The laser intensity, scan speed, and pixel averaging

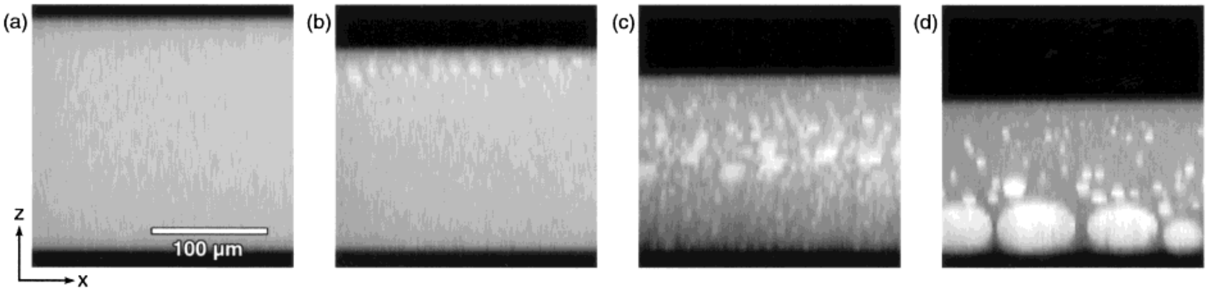

Figure 2. *xz* cross sections through a film showing the development of phase-separated microstructure during drying. Drying times are (a) 15, (b) 20, (c) 25, and (d) 25 min. Water is evaporating from the top surface.

were carefully chosen to obtain the best compromise between image stack size, acquisition time, image noise, and sample bleaching. The resulting acquisition time was slightly under 30 s per stack.

The control parameter in this work is the drying rate, Γ, which is defined as the rate of water loss per unit area of sample surface. By assuming that the volumes of the three components are simply additive, the drying rate can be calculated from the reduction of film thickness as measured directly from the microscope images. The drying rate is found to be linear and hence independent of the water concentration at the sample surface. This implies that the rate-controlling step in the drying process is the removal of water vapor from the atmosphere immediately above the sample and not the vaporization of water at the sample surface. It is also found that the drying rate is linear with the rate of air flow across the sample.

It should be noted that in these experiments, due to the surface characteristics of the Petri dishes holding the sample, the films always dewet the substrate before a solid film had formed.

Results and Discussion

The bulk of this discussion concerns the phase separation of samples with $\phi_s = 0.1$ and 0.34, both of which exhibit a droplet morphology. First we give a qualitative description of the observed morphology development, and then we present and discuss results from a quantitative analysis of the images obtained.

Figure 2 shows cross sections through a typical sample, with $\phi_s = 0.34$, at various times during the drying experiment. After 15 min of drying (Figure 2a), the composition of the sample is still in the single-phase region, and the film is a homogeneous solution. Phase separation occurs first at the surface, the bright droplets of dextran-rich material being clearly evident in the image taken after 20 min (Figure 2b). These droplets grow and, being more dense than the surrounding PEG-rich matrix, begin to sediment under the action of gravity. As drying continues, spontaneous phase separation occurs at increasing depths into the sample. After 25 min of drying, phase separation has occurred throughout the whole film (Figure 2c).

Figure 3 shows a vertical cross section and four horizontal slices through the image stack taken at 25 min. It is apparent that the droplet size varies significantly with depth through the film. In the bottom half of the film, the droplets, which have appeared recently, are small and densely packed. In contrast, in the top half of the film, the size of the droplets increases with depth, and the density is somewhat lower. The development of the structure in the upper half of the film can be understood by considering the first droplets to appear. These appeared, as we have seen, at the surface and are more dense than the surrounding PEG-rich matrix. After a short time, they have grown to a size such that gravitational forces become significant, and they start to sink through the film. As they fall, they coalesce with each other and with the smaller droplets that are forming below them, and their size increases rapidly. In the meantime, more droplets have appeared at the surface, and the process repeats itself, resulting in the structure noted above. Figure 3d clearly shows a bimodal distribution of droplets, the much larger droplets falling from above through a sea of smaller, recently nucleated droplets.

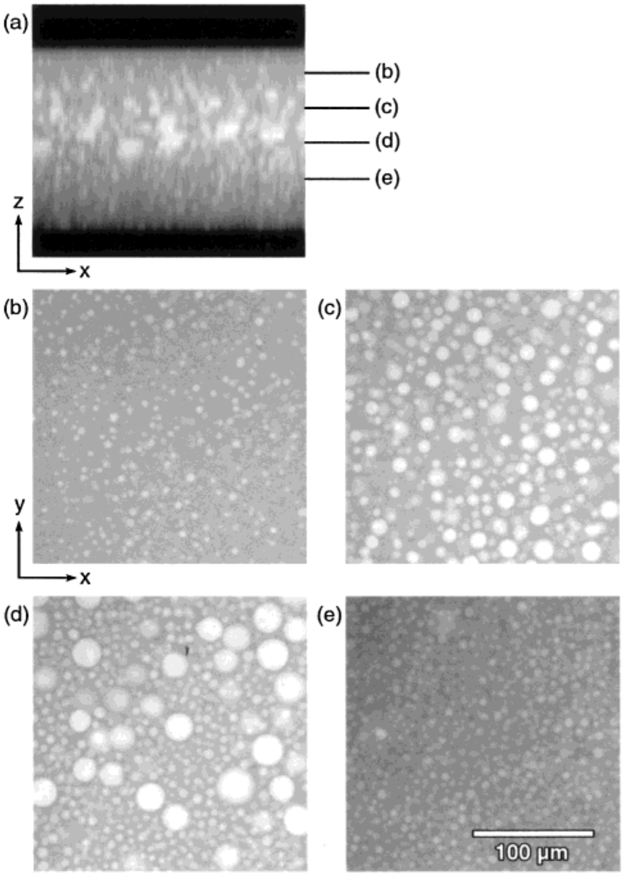

Figure 3. (a) *xz* cross section through a sample with $\phi_s = 0.34$ some time after phase separation has commenced. (b−e) *xy* sections at different depths, as marked in (a). The dextran-rich phases are bright.

Eventually, the large sinking droplets hit the bottom of the film (as seen in Figure 2d) where they continue to grow as they coalesce with each other and also with droplets falling into them from above. Nucleation of

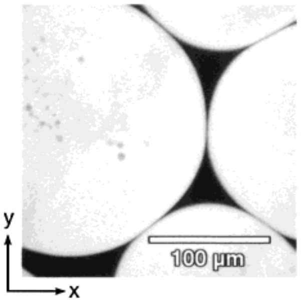

Figure 4. Horizontal section through a sample showing large dextran-rich droplets squashed together without coalescing. Small PEG-rich droplets are evident within the larger dextran-rich domains.

droplets throughout the film continues but slows down as the concentration of dextran in the matrix decreases.

At later times, dextran-rich droplets grow on the top surface of the film without sinking and with little relative movement between them. It is likely that the viscosity at the surface has become very high, effectively forming a skin and trapping the droplets. Their growth will therefore be purely diffusion-driven with no coalescence events. In contrast, the large droplets on the bottom of the film continue to grow by coalescence. However, the rate of coalescence slows dramatically, and in some cases, large droplets (>100 μm radius) are observed pressed together such that they distort one another, yet they remain stable for some time (Figure 4). This can be explained by the combination of the increasing viscosity of the matrix layer between the droplets and the decreasing driving force for coalescence as droplet size increases.

It is also evident from Figure 4 that smaller PEG-rich droplets have appeared in the large dextran-rich droplets. These are a result of secondary phase separation. As the large droplets continue to lose water, the equilibrium phase composition changes, and there is a driving force to expel PEG from the droplet. With very large droplets and high viscosities, the diffusion of PEG out of the droplets is not sufficient and so subdomains of PEG-rich material are formed within the dextran-rich droplets.

It is clear that the morphology development is strongly influenced by the effect of gravitational sedimentation. Droplet growth is dominated by coalescence of the sinking droplets with the smaller droplets below them. Another important aspect of the structure development is the gradual onset of phase separation through the film, starting at the surface and occurring at greater depths as drying progresses. Bearing in mind that phase separation will first occur when the local water content reaches a critical value, this strongly suggests that the solvent quench is inhomogeneous and that the local water content varies with depth into the film. As water is lost only from the upper surface, it is to be expected that there is a profile of water concentration through the depth of the film, the sample being depleted in water near the surface.

The vertical distribution of water in the film before phase separation occurs can be estimated by considering one-dimensional diffusion of water out of an infinite sheet.[26] The sheet initially has a uniform water concentration, C_0. The base of the sheet, at $x = 0$, is impermeable, and the top surface, at $x = l$, is subject to a constant flux of water, F_0. Ignoring the decrease in film thickness due to the loss of water, the water concentration, C, at height, x, and time, t, is given by

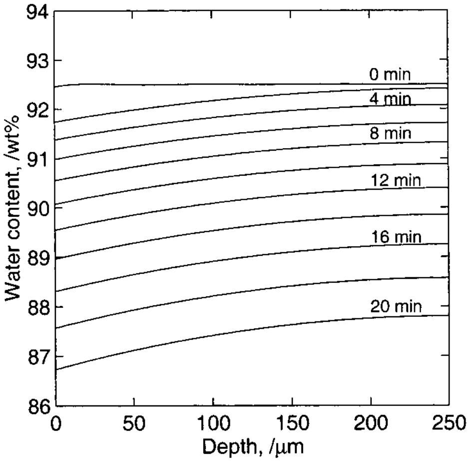

Figure 5. Water concentration profiles of a film during a typical drying experiment calculated at 2 min intervals from 0 to 20 min. The highest profile shows the initial uniform concentration, and the concentration falls as evaporation proceeds.

$$C = C_0 + \frac{F_0 l}{D}\left[\frac{Dt}{l_2} + \frac{3x^2 - l^2}{6l^2} - \frac{2}{\pi^2}\sum_{n=1}^{\infty}\frac{(-1)^n}{n^2}\exp\left(\frac{-Dn^2\pi^2 t}{l^2}\right)\cos\left(\frac{n\pi x}{l}\right)\right] \quad (1)$$

where D is the diffusion coefficient of water in the sample. D cannot easily be measured, but a reasonable approximation may be made by using the diffusion coefficient of water in a 10% glucose solution (1.66×10^{-9} m^2 s^{-1}).[27] From a typical drying experiment, the values $l = 235$ μm and $F_0 = -8.59 \times 10^{-8}$ kg m^{-2} s^{-1} were measured and used to calculate the water concentration profiles shown in Figure 5. While this is a simplistic calculation, which takes no account of the concentration dependence of D and also ignores convection, it clearly shows that a significant depletion in the water content of the sample near the surface is reasonable. These calculations also predict that the degree of depletion of water at the surface increases with drying rate. This is supported by the finding that more rapidly dried films exhibit phase separation at a higher overall water content than those dried more slowly (Figure 6).

If significant convection occurs in the sample, it would serve to equalize the diffusion imposed composition gradients, and the above calculation would be invalid. However, we believe this is not the case. The onset of thermally activated convection is identified using the Rayleigh number:[2,28]

$$Ra = \frac{\alpha \Delta T L^3 g}{\chi \nu} \quad (2)$$

where α is the thermal expansivity, ΔT is the temperature difference, L is a characteristic length scale, g is the acceleration due to gravity, χ is the thermal diffusivity ($\chi = \kappa/(\rho c_p)$, where ρ is density, κ is thermal conductivity, and c_p is the heat capacity), and ν is the kinematic viscosity. We assume that the temperature difference across the sample due to evaporative cooling is of the order 1 °C. This is an upper bound estimate

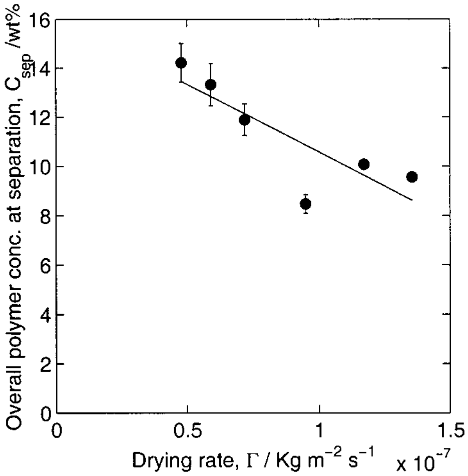

Figure 6. Drying rate dependence of the overall polymer concentration at onset of phase separation. Filled symbols are data, and the solid line is a linear fit.

based on the findings by Mitov[2] that a toluene solution of similar thickness developed a temperature difference of 0.4 °C. The solution viscosity is approximated by 3 mPa s, the viscosity of a 10 wt % PEG solution.[29] Using these values and the properties of water, we estimate the Rayleigh number in our system is around 1, which is very much lower than the critical value for convection, $Ra > 1100$.

Similarly, convection driven by interfacial tension gradients (Bénard–Marangoni convection) is usually identified using the Marangoni number:[2,30]

$$Ma = -\frac{\partial \gamma}{\partial T}\frac{\Delta T a}{\nu \rho \chi} \tag{3}$$

where $\partial\gamma/\partial T$ is the temperature derivative of the interfacial tension (0.15 mN m^{-1} K^{-1} for water[31]). Here we find that $Ma = 90$, slightly above the generally quoted threshold for instability, at $Ma = 80$. However, it has been noted that the Marangoni instability is frequently not observed until considerably higher values of Ma are reached;[30] this is due to the presence of interfacially active species. In this system PEG is interfacially active; therefore, we do not expect Bénard–Marangoni convection to occur. This is supported by our observations; in the work by Mitov[2] Bénard–Marangoni convection leads to the formation of regular arrays of phase separated droplets at the interface which are not observed in our system.

To characterize the morphologies found in these films during drying, the droplet sizes were measured as a function of depth. Each image stack was split up into a series of 2D horizontal slices, and each slice was analyzed separately using a commercial image analysis package.[32] First, a local equalization algorithm was applied to enhance contrast and remove any broad intensity variations across the field of view. A median filter was then applied to reduce noise while retaining edge detail. The droplets were delineated using an automatic intensity threshold and then identified. The area of each droplet (or, more accurately, the area of the 2D intersection of each droplet and the image plane) is measured from which the number-average droplet radius is calculated. Figure 7 shows typical data of mean droplet radius as a function of depth. It clearly shows the initial nucleation of droplets at the surface and the subsequent growth of droplets throughout the film. The increase of droplet size with depth below the surface is obvious. The peak in the mean droplet radius shows the position of the largest droplets in the film which, as we identified earlier, have grown from the first droplets nucleated at the surface. The growth and descent of these droplets can easily be followed.

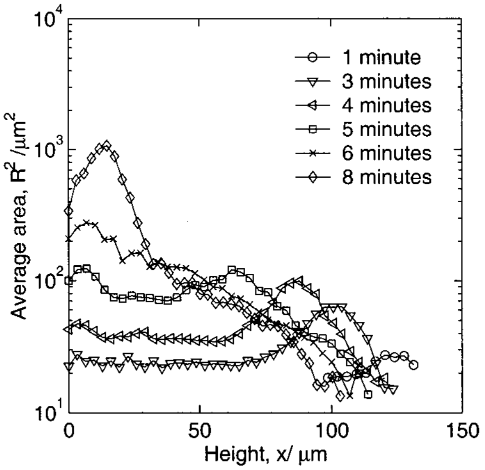

Figure 7. Mean droplet radius as a function of height above the bottom of the sample for a $\phi_s = 0.34$ sample at a drying rate of $\Gamma = 5.9 \times 10^{-8}$ kg m^{-2} s^{-1}.[1] Legend indicates the time after the onset of phase separation at which the measurement was made.

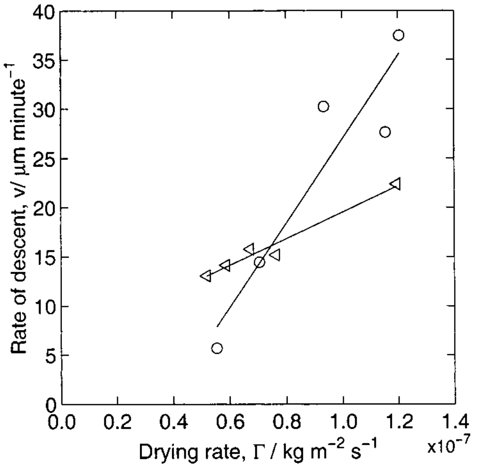

Figure 8. Drying rate dependence of the rate of descent of the largest droplets for $\phi_s = 0.34$ (△) and $\phi_s = 0.1$ (○). Solid lines are linear fits to the data.

The velocity of the peak in the droplet size is constant for the period during which the largest droplets are falling toward the bottom of the sample, thus allowing the rate of descent of these droplets to be calculated. Figure 8 shows the rate of descent of the largest droplets as a function of drying rate, for both $\phi = 0.1$ and $\phi = 0.34$. The rate of descent increases for larger drying rates with the $\phi = 0.1$ droplets falling faster than the $\phi = 0.34$ droplets at higher drying rates. For comparison, we can calculate the terminal velocity, v_T, for the sedimentation of an isolated solid sphere, used by Cau[6] and based on the behavior of a solid sphere undergoing sedimentation in a fluid is given by

$$\nu_T = \frac{2g\Delta\rho R^2}{9\eta} \tag{4}$$

The time to reach terminal velocity is of order $10\rho R^2/(9\eta)$; for our system this time is negligible ($\ll$1 s). The terminal velocity is around 145 μm min^{-1}, assuming droplets of 8 μm radius, a density mismatch of 50 kg m^{-3} (measured using a Paar densitometer), and a continuous phase viscosity of 3 mPa s. This estimate is rather higher than the observed values for the velocity of descent. At least some of the discrepancy can be accounted for by the enhancement of the suspension viscosity over the continuous phase viscosity, as described by Einstein and Batchelor.[33] They predict

$$\eta^* = \eta(1 + 2.5\phi + 6.2\phi^2) \tag{5}$$

where ϕ is the volume fraction of the suspension, η is the continuous phase viscosity, and η^* is the observed viscosity. This effect could account for approximately a halving of the estimated terminal velocity, but the effect should be much bigger for the $\phi = 0.34$ data. We note that even with extreme values of the volume fraction it cannot account for the variation of the descent velocity with drying rate. An alternative explanation is that descent rate is limited by drainage—for droplets to descend, fluid below the droplets must flow up past them. Such effects are not incorporated into the Einstein–Batchelor expression. It is to be expected that these effects are larger for higher volume fractions. This may also account for the dependence of descent rate on drying rate. At lower drying rates, it takes longer for phase separation to occur throughout the whole film, and so the volume fraction of the smaller droplets below the largest droplets is smaller.

The expected time dependence of the maximum droplet size can be deduced using a simple model. Let us assume that a droplet, radius R, has formed at the surface of the sample and has started to fall toward the bottom of the sample through a matrix which contains small droplets, radius r, with an overall phase volume ϕ_s. We assume that the big droplet will absorb each small droplet that it falls upon. If the big droplet falls by a small distance, dx, then the increase in volume of the droplet, dV, through absorbing the small droplets is given by

$$dV = dx 2\pi(r + R)^2\phi_s \tag{6}$$

dV is related to the change in radius of the big droplets; in fact, $dV = 4\pi R^2\, dR$. By substituting this into (6) and integrating, we find that

$$R - \frac{r^2}{r + R} - 2r\log(r + R) = \frac{x\phi_s}{2} \tag{7}$$

The leading term in R dominates, and so we expect $R \sim \phi_s x$. Where x is the distance from the surface, we have shown that the droplets descend at a constant velocity and so $x \sim t$. Therefore, $R \sim \phi_s t$, and we expect that plots of the maximum droplet size $R_{\max}$ vs $\phi_s t$ should be universal and scale data from different volume fractions and drying rates onto one straight line. Such a plot is shown in Figure 9. Values of ϕ_s were measured from the image stacks, although their measurement was somewhat uncertain. The proposed model takes no account of whether the droplets are the largest in the system and should apply to any of the droplets. Figure 10 shows results of measurements on droplets made below the largest ones, in the same manner as Figure 9. Although the number of data points in each series is limited, both sets of data are consistent with a linear growth rate. However, the data do not collapse onto a universal curve, and so the predicted dependence on ϕ_s is not supported. This is discussed in more detail below.

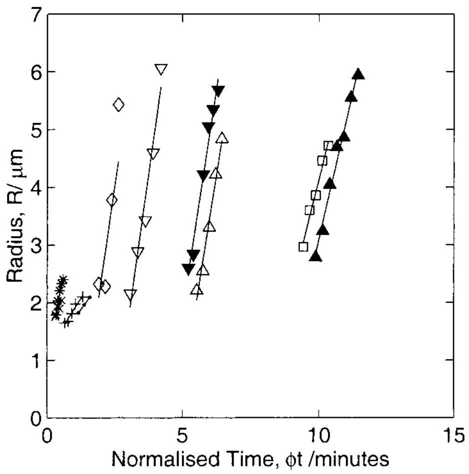

Figure 9. Maximum mean droplet radius vs ϕ t for ϕ_s = 0.34: $\Gamma = 13.5 \times 10^{-8}$ kg m^{-2} s^{-1} (◇), $\Gamma = 11.9 \times 10^{-8}$ kg m^{-2} s^{-1} (▽), $\Gamma = 6.7 \times 10^{-8}$ kg m^{-2} s^{-1} (△), $\Gamma = 5.9 \times 10^{-8}$ kg m^{-2} s^{-1} (▼), $\Gamma = 5.2 \times 10^{-8}$ kg m^{-2} s^{-1} (▲), $\Gamma = 4.7 \times 10^{-8}$ kg m^{-2} s^{-1} (□); for ϕ_s = 0.1: $\Gamma = 12.0 \times 10^{-8}$ kg m^{-2} s^{-1} (×), $\Gamma = 9.3 \times 10^{-8}$ kg m^{-2} s^{-1} (∗), $\Gamma = 7.1 \times 10^{-8}$ kg m^{-2} s^{-1} (+), $\Gamma = 5.55 \times 10^{-8}$ kg m^{-2} s^{-1} (●). Solid lines are linear fits to the data.

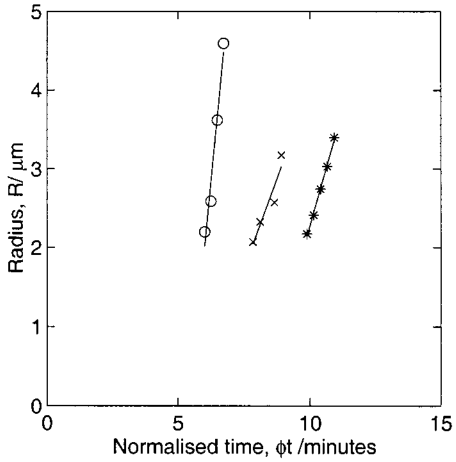

Figure 10. Mean droplet radius vs ϕt for droplets lower in the sample than the largest droplets, all with ϕ_s = 0.34 and drying rates $\Gamma = 6.7 \times 10^{-8}$ kg m^{-2} s^{-1} (○), $\Gamma = 5.9 \times 10^{-8}$ kg m^{-2} s^{-1} (×), and $\Gamma = 5.2 \times 10^{-8}$ kg m^{-2} s^{-1} (∗). Solid lines are linear fits to data.

We note that, for moderately concentrated systems, Siggia[34] predicts a linear growth regime, in the absence of gravity, based on dimensional analysis and qualitative arguments of a hydrodynamic nature. Furthermore, both the droplet collision mechanism proposed by Binder and Stauffer[35] and the coarsening of droplets by diffusion as described by Liftshitz and Slyozov[36] produce a linear growth rate in the late stages of phase separation.

Extrapolating the linear fits in Figure 9 back to the time at which phase separation was first observed gives a finite initial droplet size which appears to be independent of drying rate and in the region 1.8 μm < r < 2.5 μm. We can interpret this nonzero intercept as indicating that there is a critical size beyond which droplets must grow before they start to sediment. This critical size can be estimated by balancing the thermal

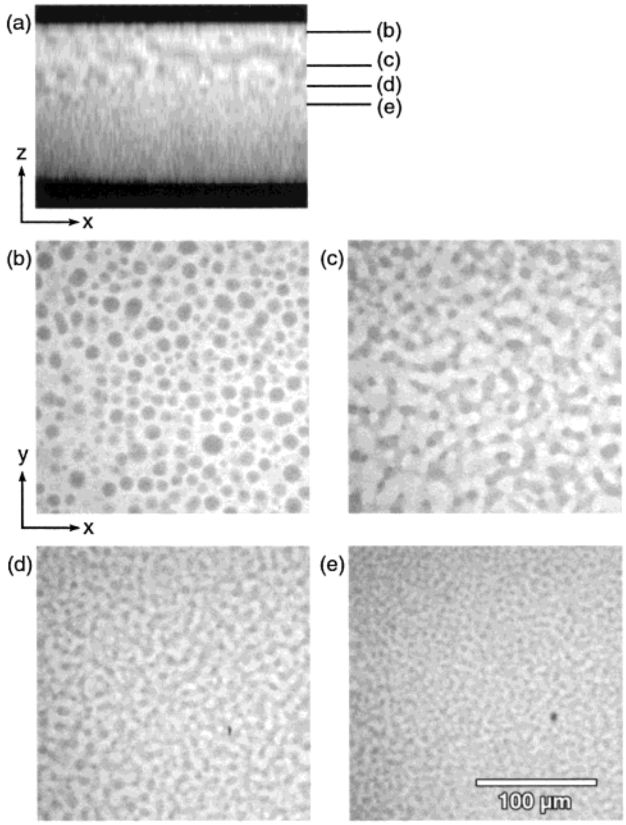

Figure 11. Bicontinuous morphology for $\phi_s = 0.5$, 2 min after the onset of phase separation: (a) $x-z$ section, (b−e) $x-y$ sections at the positions marked in (a). Bright areas are the dextran-rich phase.

energy of the droplets to their gravitational potential energy, i.e.

$$\frac{3}{4}k_B T = \frac{4}{3}\pi r^3 \Delta\rho g h \tag{8}$$

where r is the critical droplet radius, $\Delta\rho$ is the difference in density between the phases, g is the acceleration due to gravity, T is the temperature, k_B is the Boltzmann constant, and h is the height through which a droplet must fall for sedimentation to be considered significant. In this system it seems reasonable to approximate $h = 1\ \mu$m, giving a value of $r_{crit} \approx 1.4\ \mu$m, which is broadly consistent with the observed intercept behavior.

While plots of R_{max} vs $\phi_s t$ are linear they do not collapse onto a common line, suggesting that the model oversimplifies the matrix through which the droplets are falling. This is unsurprising since we have taken no account of the possible hydrodynamic interactions in the system. In particular a "coalescence induced coalescence" mechanism[37,38] has been proposed, in which droplet coalescence causes hydrodynamic flows leading to further coalescence. This means that the "effective" volume fraction of material through which a droplet is falling differs from the measured volume fraction ϕ_s.

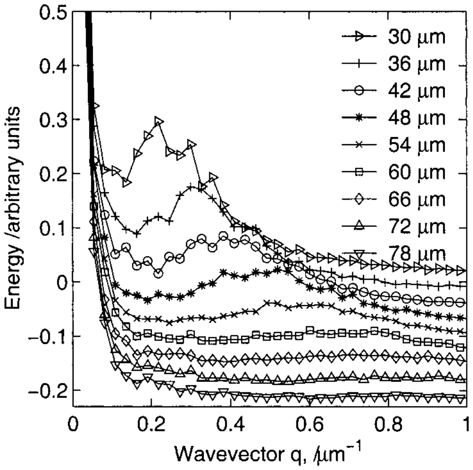

Figure 12. Radially averaged FFT's of $x-y$ sections of the bicontinuous morphology for the sample shown in Figure 11. Data from successive slices are offset for clarity.

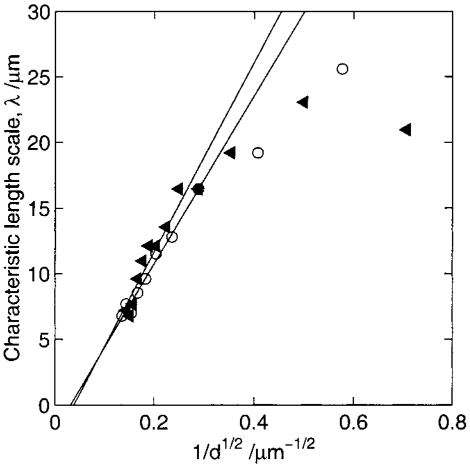

Figure 13. Characteristic length scales obtained from the positions of the maxima in the radially averaged FFT's shown in Figure 12, plotted as a function of $1/d^{1/2}$ where d is the distance from the air surface.

At dextran volume fractions $\phi_s = 0.5$, a bicontinuous morphology is observed, as is anticipated from a wide body of literature. In contrast to systems subjected to a homogeneous quench, this system exhibits a bicontinuous structure whose length scale varies with depth into the sample. This is illustrated in Figure 11, which shows $x-y$ planes at selected distances from the surface along with an $x-z$ plane. A very thin surface layer consists of PEG-rich droplets. Whether this is the result of the breakup of the bicontinuous structure or whether the morphology is affected by the sample−air interface is unclear. The graded bicontinuous structure is seen shortly (within 1−2 min) after the first signs of phase separation. It rapidly disappears as the sample coarsens by gravity-induced drainage of the bicontinuous phases. This leads to further heterogeneous structures with areas that are bicontinuous and others that are PEG-rich droplet phases or dextran-rich droplet phase.

We can obtain a measure of the characteristic length scale of the graded bicontinuous structure by applying a 2D FFT to individual $x-y$ planes in the sample. This resulting transforms are analogous to static light scattering patterns and are circularly symmetric, exhibiting a maximum intensity as a function of q. The position of the maxima in the transforms shifts to higher q with increasing depth from the drying surface, d, as illustrated in Figure 12. Characteristic length scales are obtained from the positions of the maxima. The variation of characteristic length scale with $d^{-1/2}$ for two identical samples is illustrated in Figure 13.

The variation of length scale with depth can be rationalized by making the following assumptions. Phase separation will be initiated when the local water content reaches a critical concentration. The water concentration profile normal to the surface is expected to have a length scale that varies as the square root of time, as is consistent with a diffusion process. As we are observing the late-stage coarsening region of phase separation, the growth of the characteristic length scale should be linear with time. Consequently, we expect the characteristic length scale to vary as 1/(const + $d^{1/2}$), and hence the plots of length scale vs $d^{-1/2}$ (Figure 13) should be linear as long as the constant is small.

Deviations from linearity are likely to occur at small depths, corresponding to large $d^{-1/2}$, where the size of the constant will be large compared to the depth. Examining Figure 13, we see that the data are consistent with such assumptions with a linear region at small $d^{-1/2}$ and deviations at higher $d^{-1/2}$. The lines on the figure are linear fits to all but the two smallest depth values, constrained to pass through the origin. Clearly, there are insufficient data to be absolutely confident that these simple arguments embody the key physical processes at work in the system, but they at least provide a plausible explanation of the observed data. The graded structure is only observed at times shortly after phase separation has started and before significant density driven sedimentation can take place so it is not necessary to consider such effects in our crude model of the observed length scale.

Conclusions

We have measured quantitatively the morphology development in a ternary polymer mixture undergoing phase separation, induced by solvent loss, using confocal microscopy. As expected, the behavior is strongly influenced by gravitational sedimentation and by the inhomogeneous nature of the quench. Solvent loss by evaporation from the upper surface leads to a variation in local water concentration through the depth of the sample, the water content being lower nearer the upper surface. Phase separation thus occurs initially at the surface and then gradually at greater depths as drying continues. The resulting transient structures show considerable variation with depth into the sample for both droplet and bicontinuous morphologies. Confocal microscopy is an excellent tool for observing such complex structures in three dimensions and, when combined with standard image analysis tools, can yield quantitative information about the structures and their development.

At volume fractions of the dextran-rich phase, ϕ_s = 0.1 and 0.34 droplet morphologies were observed with phase separation commencing at the upper surface of the sample. The resulting droplets sediment through the sample under the action of gravity and grow by coalescence with smaller droplets that recently formed below them. The growth law was found to be linear in time, which could be justified using a simple collision argument. At volume fractions of dextran $\phi_s = 0.5$, a bicontinuous structure was observed in which the characteristic length scale decreased with increasing distance from the upper, drying surface. This behavior results from the range of times at which phase separation initiates because of the profile of water concentration.

Although simple models can be used to describe the broad character of phase separation behavior observed, there are details, particularly in the drying rate dependence of the growth rate, which are not understood.

Acknowledgment. We thank Brad Thiel for his many helpful suggestions, and we are grateful to Unilever plc and EPSRC for funding this work.

References and Notes

(1) Kumacheva, E.; Li, L.; Winnik, M. A.; Shinozaki, D. M.; Cheng, P. C. *Langmuir* **1997**, *13*, 2483−2489.
(2) Mitov, Z.; Kumacheva, E. *Phys. Rev. Lett.* **1998**, *81*, 3427−3430.
(3) Serrano, B.; Baselga, J.; Bravo, J.; Mikes, F.; Sese, L.; Esteban, I.; Pierola, I. F. *J. Fluoresc.* **2000,** *10*, 135−139.
(4) Müller-Buschbaum, P.; Gutmann, J. S.; Wolkenhauer, M.; Kraus, J.; Stamm, M.; Smilgies, D.; Petry, W. *Macromolecules* **2001**, *34*, 1369−1375.
(5) To, K. W.; Chan, C. K. *Europhys. Lett.* **1992**, *19*, 311−316.
(6) Cau, F.; Lacelle, S. *Phys. Rev. E* **1993**, *47*, 1429−1432.
(7) Puri, S.; Binder, K.; Dattagupta, S. *Phys. Rev. B* **1992**, *46*, 98−105.
(8) Lacasta, A. M.; Hernández-Machado, A.; Sancho, J. M. *Phys. Rev. B* **1993**, *48*, 9418−9425.
(9) Chan, C. K.; Goldburg, W. I. *Phys. Rev. Lett.* **1987**, *58*, 674−677.
(10) Kono, K.; Ishizuka, T.; Tsuda, H.; Kurosawa, A. *Comput. Phys. Commun.* **2000**, *129*, 110−120.
(11) Swift, M. R.; Osborn, W. R.; Yeomans, J. M. *Phys. Rev. Lett.* **1995**, *75*, 830−833.
(12) Assenheimer, M.; Khaykovich, B.; Steinberg, V. *Physica A* **1994**, *208*, 373−393.
(13) Platten, J. K.; Chavepeyer, G. *Phys. Lett. A* **1993**, *174*, 325−328.
(14) Wilson, T., Ed. *Confocal Microscopy*, 1st ed.; Academic Press: London, 1990; p 426.
(15) Chestnut, M. H. *Curr. Opin. Colloid Interface Sci.* **1997**, *2*, 158−161.
(16) Ribbe, A. E. *Trends Polym. Sci.* **1997**, *5*, 333−337.
(17) Blaaderen, A. v.; Wiltzius, P. *Science* **1995**, *270*, 1177−1179.
(18) Kegel, W. K.; Blaaderen, A. v. *Science* **2000**, *287*, 290−293.
(19) Ribbe, A. E.; Hashimoto, T. *Macromolecules* **1997**, *30*, 3999−4009.
(20) Ribbe, A. E.; Hayashi, M.; Weber, M.; Hashimoto, T. *Polymer* **1998**, *39*, 7149−7151.
(21) Jinnai, H.; Yoshida, H.; Kimishima, K.; Funaki, Y.; Hirokawa, Y.; Ribbe, A. E.; Hashimoto, T. *Macromolecules* **2001**, *34*, 5186−5191.
(22) Jinnai, H.; Nishikawa, Y.; Morimoto, H.; Koga, T.; Hashimoto, T. *Langmuir* **2000**, *16*, 4380−4393.
(23) Jinnai, H.; Koga, T.; Nishikawa, Y.; Hashimoto, T.; Hyde, S. T. *Phys. Rev. Lett.* **1997**, *78*, 2248−2251.
(24) Takeno, H.; Iwata, M.; Takenaka, M.; Hashimoto, T. *Macromolecules*, in press.
(25) Zaslavsky, B. Y. *Aqueous Two-Phase Partitioning*; Marcel Dekker: New York, 1995.
(26) Crank, J. *The Mathematics of Diffusion*; Oxford University Press: Oxford, 1975.
(27) Luyben, K. C. A. M.; Olieman, J. J.; Bruin, S. Concentration dependent diffusion coefficients derived from experimental drying curves. In *Drying '80*; Musumda, A. S., Ed.; Hemisphere Publishing Corporation: New York, 1980; pp 233−243.
(28) Faber, T. E. *Fluid Dynamics for Physicists*; Cambridge University Press: Cambridge, 1995.
(29) Brandrup, J., Immergut, E. H., Grulke, E. A., Eds. *Polymer Handbook*, 4th ed.; John Wiley & Sons: Chichester, 1999.
(30) Miller, C. A.; Neogi, P. *Interfacial Phenomena−Equilibrium and Dynamic Effects*; Marcel Dekker: New York, 1985.
(31) Kaye, G. W. C., Laby, T. H., Eds. *Tables of Physical and Chemical Constants*, 16th ed.; Longman: London, 1995.
(32) Media Cybernetics, *Image-Pro Plus*, 1997.
(33) Hunter, R. J. *Foundations of Colloid Science*; Oxford University Press: Oxford, 2001.
(34) Siggia, E. D. *Phys. Rev. A* **1979**, *20*, 595−605.
(35) Binder, K.; Stauffer, D. *Phys. Rev. Lett.* **1974**, *33*, 1006−1009.
(36) Lifshitz, I. M.; Slyozov, V. V. *Phys. Chem. Solids* **1961**, *19*, 35−50.
(37) Tanaka, H. *Phys. Rev. Lett.* **1994**, *72*, 1702−1705.
(38) Nikolayev, V. S.; Beysens, D.; Guenoun, P. *Phys. Rev. Lett.* **1996**, *76*, 3144−3147.

MA012244P